PCCP

Accepted Manuscript

ROYAL SOCIETY OF CHEMISTRY

www.rsc.org/pccp

Graphene/Nano-Porous Silicon and Graphene/Bimetallic Silicon Nanostructures (Pt-M, M: Pd, Ru, Rh), Efficient Electrocatalysts for Hydrogen Evolution Reaction

Ali A. Ensafi*, Mehdi Jafari-Asl, Behzad Rezaei

Department of Analytical Chemistry, Faculty of Chemistry, Isfahan University of Technology, Isfahan 84156–83111, Iran

Abstract

In this work first Nano-porous silicon flour (Nano-PSiF) was synthesized and the electrocatalytic activity of that investigation for electrochemical hydrogen evolution reaction (HER). The results showed that Nano-PSiF has good electrocatalytic activity for HER compare with PSiF. In the second section, Pt and Pt-M (M= Pd, Rh, Ru) bimetallic silicon nanostructures were prepared by direct reduction of the metal (Pt, Pt-Pd, Pt-Rh and Pt-Ru) on the surface PSiF by galvanic exchange mechanism. The electrocatalytic activity of the bimetallic silicon nanostructures (Pt-M/PSiF) were evaluated for HER. The results showed that all of the Pt-M/PSiFs have excellent electrocatalytic activity for HER in 0.5 mol L^{-1} H_2SO_4 solution. A bout Pt/PSiF, Tafel slope of Pt/PSiF was 46.9 mV/decade, indicating its excellent electrocatalytic activity for HER and it is comparable with commercial Pt/C. On the other hand, bimetallic silicon nanostructures showed better electrocatalytic activity than Pt/PSiF for HER (lower Tafel slope, and higher α). Finally, exfoliated graphene oxide was electro-deposited on the surface of a glassy carbon electrode (eRGO/GCE) and used as a sub-layer for Pt-M/PSiF. Then, the electrocatalytic activities of the bimetallic silicon nanostructures on eRGO/GCE were investigated for HER. Results showed that higher electrocatalytic activity of Pt-M/PSiF–eRGO/GCE compare with Pt-M/PSiF–GCE.

Corresponding author. Tel.: +98 31 33912351; Fax: +98 31 33912350; E–mail: Ensafi@cc.iut.ac.ir, aaensafi@gmail.com, ensafi@yahoo.com.

Keywords: Nano-Porous Silicon Flour; Bimetallic Silicon Nanostructures; Electrochemical Hydrogen evolution reaction.

1. Introduction

Hydrogen has been proposed as a comer energy carrier that could be used to vigor up electronic devices, vehicles and homes. [1–3] Molecular hydrogen (H_2) has the highly potential candidate for green energy because it's environmentally safe and its high energy per unit mass. It's not produce greenhouse gases and other harmful chemical compounds after burning. [4–6] Hydrogen is generated from carbon fossil fuels or water.[7–9] Water splitting is one of the helpful methods to generate H_2.[10,11] Eligible electrocatalysts should have several properties such as, nanoscale dimension to reach the maximize number of exposed active sites, high aspect ratio to improve catalytic activity per geometric area, porous structure to enhance fast mass transport of reactants and products, good electrical conductivity to facilitate electronic transfer and unique physicochemical nature to give high intrinsic catalytic activity towards electrocatalyst.[12, 13]

An advanced catalyst for the electrochemical hydrogen evolution reaction (HER) should reduce the over-potential and consequently increases the efficiency of this important electrochemical process. One of the most effective HER electrocatalysts is Pt metal.[14,15] Although platinum shows highest activity for HER however, applications of Pt catalysts are limited due to their high cost and low affluence.[16–18] Recently, new electrode materials have been investigated, intend at the reduction of the cost associated more and more scramble has been focused on Pt–based bimetallic catalysts, [19–22] because they can offer significant improvement in the catalytic properties relative to the separate and individual metal. Among these materials Ru, Rh, and Pd have lower cost than Pt. Combination of Pt with these elements (bimetallic systems) are regarded as ideal catalysts for the electrochemical

generation of hydrogen from aqueous solutions. However, regarding the high cost of direct use of these metals or thin films of the metals led to intensive investigations on molecular-based catalysts those are capable of catalyzing proton reduction at low over-potentials. [23–26] A good support should not only provide high precision catalyst nanoparticles and good electron transfer but also increase long-term consistency of the catalyst nanoparticles by slowing down their sintering rate and allowing fast mass transport of reactants and products at the fuel cell electrodes, resulting in better device performance. [27, 28]

Several theoretical studies have been reported to clear the mechanism of electrochemical water splitting at Si nanocrystal.[29] Much of them have been focused on the symptom why some metals, like Pt, show very rapid electron transfer. Two stages mechanism, Volmer-Tafel and Volmer-Heyrovsky, have been generally accepted. However, it is not clear how hydrogen generate at the surface of semiconductors, such as Si and SiC, where water molecules spontaneously dissociate at Si–H and Si–OH bonds. The theoretical studied showed that a hydronium ion adsorb at Si–H site, and when a substrate electron is driven to this complex by the applied bias voltage, an H_2 is generated. This reaction leaves behind a Si dangling bond that, under operating conditions, easily traps an electron and then reacts with another hydronium ion in solution, recreating the Si–H bond. Such mechanism is related to the Vollmer-Heyrovsky mechanism on metal electrodes, but Heyrovsky step was happening first and Volmer step was happening later at the Si surface. On the other hand, the Volmer reaction is a one-step process on metal surfaces, whereas it occurs in a two-step fashion at Si surface. It has been shown that a Si–H bond at Si–SiO_2 interface breaks when approached by a proton, an H atom binds to the proton to form an H_2 molecule.[30, 31] Although silicon semiconductors have been applied for photo-electrochemical application of water splitting, but based our knowledge, there is not any report about the experimental application of silicon nanostructure for electrochemical HER. [32,33]

In this paper, first, nano-porous pore were synthesized at the surface of silicon flour (Nano-PSiF) based on chemical etching method. Additionally, Pt and Pt-M (M = Pd, Rh, Ru) bimetallic silicon nanostructures were prepared by direct reduction of the metal of Pt, Pt-Pd, Pt-Rh and Pt-Ru on the surface of PSiF by galvanic exchange mechanism. The structure of Nano-PSiF and the bimetallic silicon nanostructures (Pt, Pt-Pd, Pt-Ru, and Pt-Rh), named as Pt-M/PSiF, were characterized by transmission electron microscopy (TEM), field emission scanning electron microscopy (FE–SEM), energy dispersive X–ray spectroscopy (EDS), X–ray photoelectron spectroscopy (XPS), X–ray diffraction techniques (XRD) and electrochemical methods. Then, the syntactic electrocatalysts were used for HER with low over-potential and appropriate Tafel slopes. Finally exfoliate graphene oxide was electro-deposited on the surface of a glassy carbon electrode (eRGO/GCE) as a sub-layer for the Nano-PSiF and Pt-M/PSiF. Then, investigate electrocatalytic activity of those combinations for HER, in 0.5 mol L^{-1} H_2SO_4 solution, with satisfactory results.

2. Experimental

2.1. Reagents

Graphite, nitric acid, hydrofluoric acid, potassium hexachloroplatinate, potassium tetrachloropalladate(II), ruthenium(III) chloride hydrate and rhodium(III) chloride hydrate were purchased from Merck. Nafion solution (5.0 wt.% in lower aliphatic alcohols and water) and polycrystalline Si Flour (325 meshes, 99%) were purchased from Aldrich. All other chemicals used in this investigation were of analytical grade and were purchased from Merck. Doubly distillate water was used for preparation of all of solutions.

2.2. Apparatus

To check the morphologies and compositions of the synthetic silicon nanostructures, TEM measurements were conducted on a Philips/FEI CM200 operating at 200 kV, FE–SEM and EDS experiments were carried out with a Philips XL–30 FE–SEM with accelerating voltage of 20 kV. XPS was performed on a PHI 5000 Versa Probe (ULVAC PHI) and Raman spectra were acquired using a Renishaw inVia, with excitation wavelength of 514.5 nm. XRD analyses were carried out with a Bruker D_8/Advance X–ray diffractometer with Cu–K_a radiation. Fourier transform IR spectra were recorded using a JASCO FT–IR (680 plus) spectrometer and the vibrational transition frequencies are reported in wavenumber (cm^{-1}).

Electrochemical investigations were done with an Autolab electrochemical analyzer, Model PGSTAT 30 potentiostat/galvanostat (Eco–Chemie, the Netherlands), that controlled by a microcomputer for all voltammetry and electrochemical impedance spectroscopy. Data were acquired and processed using GPSE computrace software 4.9.007. A standard three-electrode cell contained a platinum wire auxiliary electrode, a saturated Ag/AgCl reference electrode ($KCl_{sat'd}$) and Nano-PSiF/GCE, Pt-M/PSiF-GCE, and/or Pt-M/PSiF-eRGO/GCE (M: Pd, Ru, Rh) as working electrodes were used in the electrochemical studies.

2.3. Synthesis and Electrochemical Reduction of Exfoliated Graphene Oxide

Graphene oxide was prepared from graphite powders using a modification of Hummers method. [34] In a typical reaction, 0.50 g of graphite, 0.50 g $NaNO_3$ and 30 mL of conc. H_2SO_4 were stirred together in an ice bath. Next, 4.0 g $KMnO_4$ was slowly added to the mixture. Once mixed, the mixture was transferred to a 5 °C water bath and stirred for one hour, forming a thick paste. Next, 40 mL water was added to the mixture and stirred for 30 min, while the temperature was raised to 90 °C. Finally, 5.0 mL H_2O_2 (30%) was added to the mixture (turning the color of the solution from dark brown to yellow). The warm

mixture was then filtered and washed with 5.0 wt% HCl aqueous solution and repeatedly was washed with deionized water until the pH of the filtrate became neutral. The product was then dried at room temperature. Finally, the graphene oxide was dispersed in water (0.5 mg mL^{-1}) and placed in an ultrasonic bath for 2 h to convert to exfoliated graphene oxide (EGO).[34]

Electrochemical deposition was carried out in a carbonate buffer solution (pH 9.2) containing 0.5 mg mL^{-1} EGO with running cyclic voltammogram (CV) under stirring for ten cycles from +0.60 to –1.60 V and with scan rate 25 mV s^{-1}. It is widely accepted that the peak at ca. −1.40 V is ascribed to the irreversible electrochemical reduction of EGO. The continuous increasing in the peaks current with successive CV scans indicated that EGO was successfully convert to reduced graphene oxide, and attached onto the glassy carbon electrode surface (eRGO/GCE).[35]

2.4. Synthesis of Nano-Porous Silicon and Pt-M Silicon Nanostructures (M: Pd, Ru, Rh)

Nano-PSiF was prepared by chemical etching method. Commercially available polycrystalline Si–Flour was dispersed in an etching solution consisted of HF, HNO_3 and H_2O with molar ratio of 6:1:30, respectively for 20 min. Then, it was rinsed with water and dried at room temperature for 24 h. After the chemical etching, the initially metallic color of the powder was changed to brown-yellow for the porous silicon flour. Synthesis of Nano-PSiF was done by an electroless Ag deposition from 2.0 mmol L^{-1} $AgNO_3$ in 1.0 wt% HF solution for 6 min, followed by rinsing with water and drying at room temperature. Finally, the deposited Ag nanoparticles on the surface of the porous silicon were removed by soaking it in a 32 wt% HNO_3 solution for 30 min to prepare Nano-PSiF.[36]

To synthesis Pt, Pt-Pd, Pt-Rh and Pt-Ru silicon nanostructures, 0.250 g PSiF was immersed in a solution of 20.0 mmol L^{-1} K_2PtCl_6 (to synthesis Pt/PSiF), 10.0 mmol L^{-1}

K_2PtCl_6 plus 10.0 mmol L^{-1} K_2PdCl_4 (to synthesis Pt-Pd/PSiF), 10.0 mmol L^{-1} K_2PtCl_6 plus 10.0 mmol L^{-1} $RuCl_3$ (to synthesis Pt-Ru/PSiF), and/or 10.0 mmol L^{-1} K_2PtCl_6 plus 10.0 mmol L^{-1} $RhCl_3$ (to synthesis Pt-Rh/PSiF) in 1.0 wt% HF solution for 6 min, followed by rinsing with water and dried at room temperature for 24 h.[37]

3.Results and discussion

3.1. Characterization of Exfoliated Graphene Oxide and Reduce Graphene Oxide

Before the electro-deposition of exfoliated graphene oxide on the surface of GCE, it was characterized by different methods such as TEM, EDS, FT–IR and Raman spectroscopy. Fig. 1A shows TEM image of exfoliated graphene oxide, whereas Fig. 1B shows the EDS results. The EDS peaks reveal the presence of 61.59% (w/w) C and 38.41% O. These results demonstrated that exfoliated graphene oxide was successfully synthesized. Fig. 1C shows a typical cyclic voltammograms for the reduction of EGO to eRGO at the surface of GCE in carbonate buffer solution (pH 9.2), where one anodic peaks (I) and two cathodic peaks (II and III) are increasing during the reduction process. The sequential increasing in the peak currents with successive potential scans demonstrated that the successive deposition of conducting eRGO on the surface of GCE. Moreover, the anodic peak I and cathodic peak II were ascribed to the redox pair of some electrochemically active oxygen-containing groups on the graphene planes; those are too stable at the electrode surface to be reduced by cyclic voltammetry method. On the other hand, the cathodic peak current (III) is attributed to the irreversible electrochemical reduction of EGO.[35] EGO is well dispersed in the solution at pH 9.2 (carbonate buffer), whereas eRGO (the resulted graphene sheets) is also insoluble, and thus directly attach to the electrode surface. "**Here Fig. 1"**

Cyclic voltammograms of different electrodes in 5.0 mmol L^{-1} $Fe(CN)_6^{3-/4-}$ (containing 0.1 mol L^{-1} KNO_3) were recorded (Fig. 2A). The unmodified GCE shows a pair

of well-defined voltammetric peaks with a cathodic peak potential (E_{pc}) of –0.05 V and an anodic peak potential (E_{pa}) of +0.38 V and with peak-to-peak separation (ΔE_p) of 0.43 V, whereas eRGO modified-GCE shows a pair of well-defined voltammetric peaks with peak-to-peak separation of 0.25 V. The voltammograms showed that the peak-to-peak potential separation of eRGO-GCE is lower than unmodified GCE, whereas the peak current of eRGO-GCE significantly higher. Therefore, the improved performance demonstrated faster electron transfer and larger electroactive surface area of eRGO modified-GCE *vs.* unmodified-GCE. These results also indicated that the ferrocyanide electrochemistry at the unmodified-GCE and eRGO/GCE mainly took place within a 3D porous electrode structure.

AC impedance spectroscopy was also used to study eRGO/GCE behavior (Fig. 2B). The Nyquist diagrams of the electron transfer kinetics for the redox probe (in 10 mmol L^{-1} $[Fe(CN)_6]^{3-/4-}$) at unmodified-GCE and eRGO/GCE showed that the charge transfer resistance of the eRGO/GCE remarkably is lower than GCE.

FT–IR and Raman spectroscopy were used to examine the reduction degree of the eRGO (Figs. 2C and 2D). FT–IR spectrum of EGO showed the characteristic absorption bands corresponding to the stretching of OH groups of carboxyl (O–H), carbonyl groups (C=O), epoxy (C–O–C and C–O) and C=C groups.[38] After electrochemical reduction of EGO to eRGO, the intensities of most of the absorption bands reduced or disappeared. For example, the peak intensity of C=O (1741 cm^{-1}) reduces and the peak for C–O–C (epoxy 1100 cm^{-1}) disappeared, whereas the peak intensity of C=C (1618 cm^{-1}) increases, which proved the effective elimination of the oxygen and synthesis of the reduce graphene oxide. Raman spectrum of EGO contained both G and D bands at 1355 cm^{-1} and 1595 cm^{-1}, respectively. After electrochemical reduction of EGO, the intensity of G bond increased, confirmed that EGO successfully converted to eRGO. Formation of eRGO film on the GCE

surface was directly confirmed by the SEM conducting surfaces too (Fig. 2E). Moreover, the graphene coating is very stable as a result of its poor insolubility in common solvents.

"Here Fig. 2"

3.2. Physical and Electrochemical Characterization of the Silicon Nanostructures

Presence of HF in the electro-less displacement is essentially factor for the corrosion reaction (at the silicon surface), which is in conjugate with the metal deposition on the silicon surface. This acts as a source of electrons that reduces a metal ion to $M^{(0)}$ (in solution) on the silicon surface, while the surface atoms are oxidized and solubilized either locally and/or distally from an exposed surface.[36] In the case of silicon, hydrofluoric acid is required to ensure continuous metallic growth since the spontaneously formed silicon oxide product is a dielectric, and would prevent further metal ion reduction. In the presence of $HF_{(aq)}$, the silicon oxide layer is dissolved in-situ to form soluble $SiF_6^{2-}{}_{(aq)}$ species and the metal ions were reduced spontaneously, according to the following equations:

$$SiF_6^{2-} + 4e^- \longrightarrow Si_s + 6F^- \qquad E^\circ_{SiF^{6-}/Si} = -1.20\ V\ vs.\ NHE \qquad (1)$$

$$AgNO_3 + e^- \longrightarrow Ag^\circ_s + NO_3^- \qquad E^\circ_{Ag+/Ag^\circ} = +0.8\ V\ vs.\ NHE \qquad (2)$$

$$PtCl_6^{2-} + 4e^- \longrightarrow Pt^\circ_s + 6Cl^- \qquad E^\circ_{Pt^{4+}/Pt^\circ} = +1.42\ V\ vs.\ NHE \qquad (3)$$

$$PdCl_4^{2-} + 2e^- \longrightarrow Pd^\circ_s + 4Cl^- \qquad E^\circ_{Pd^{2+}/Pd^\circ} = +0.76\ V\ vs.\ NHE \qquad (4)$$

$$RhCl_3 + 3e^- \longrightarrow Rh^\circ_s + 3Cl^- \qquad E^\circ_{Rh^{3+}/Rh^\circ} = +0.76\ V\ vs.\ NHE \qquad (5)$$

$$RuCl_3 + 3e^- \longrightarrow Ru^\circ_s + 3Cl^- \qquad E^\circ_{Ru^{3+}/Ru^\circ} = +0.70\ V\ vs.\ NHE \qquad (6)$$

Different methods including FT–IR, TEM, FE-SEM, XRD, XPS and BET were used to investigate the characteristics of Ag/PSiF, and Nano-PSiF.

The morphology of the Ag/PSiF nanostructure was studied by means of FE–SEM. Fig. 3A shows a typical cross-sectional SEM image of the Ag/PSiF nanostructure. These images showed that Ag nanoparticles are well distributed on the surface of PSiF. Dissolving of Ag nanoparticles from Ag/PSiF nanostructures in HNO_3, cause changing the morphology of the PSiF to Nano-PSiF. The stain etching of the nano-porous silicon flour results in an open sponge-like structure consisting of nanometers range pores on the porous silicon flour those can be seen in HR-TEM image in Fig. 3C. From the HR-TEM image, the size of the pore on the silicon flour, could be estimated to be less than 20–30 nm.

The surface termination of Nano-PSiF supports has a significant influence on their reductive potential. Instability of hydrogen termination of Nano-PSiF under heat treatment or strong oxidizing conditions was reported earlier.[39] Ag-replacement method (that is used here) causes stable hydrogen termination on Nano-PSiF surfaces. FT–IR spectrum of a typical Nano-PSiF sample (exposed to air) dominating surface groups identified spectra of Si–H, Si–H_2 and Si–H_3. Si–H bending (625 cm^{-1}) and Si–H_2 wagging (662 cm^{-1}) vibration modes were observed for these different types of Nano-PSiF. The stretching modes of Si–H_x bonds (for x = 2 and 3 are 2050 cm^{-1} and 2285 cm^{-1}, respectively) were also observed.[40] A feature related to the Si–O–Si asymmetric stretching mode (1272 cm^{-1}), caused by surface oxidation of Nano-PSiF on air, can also be clearly seen in the result spectra as shown in Fig. 3C.

The XRD patterns of Nano-PSiF are illustrated four diffraction peaks at $2\theta = 28.5^{o}$, 47.1^{o}, 56.0^{o}, 69.0^{o} for Si (221), Si (311), Si (400), Si (331), respectively (results not shown). XPS reveals significant differences between commercial silicon flour and Nano-PSiF. Figure 3D compares the binding energy for the commercial silicon flour and Nano-PSiF. The maxim are normalized in order to clearly distinguish the position of the peak maxima. This figure clearly shows that the Si2p peaks are shifted to higher energies for Nano-PSiF

compare to the commercial silicon flour, due to changes in the chemical environment. This shift could be associated with increasing SiHx species with porosity (related with a blue-shift of photoluminescence for microporous).[1] **"Here Fig. 3"**

The EDS results confirm presence of 92.54% (w/w) Si and 7.46% Ag at Ag/PSiF, whereas after dissolving the Ag nanoparticles in HNO_3 solution, the amount of Si converted to 99.65% Si. These results demonstrated that Ag/PSiF and Nano-PSiF were successfully synthesized. The estimated BET surface area of the PSi flour was 15.3 m^2 g^{-1}, whereas for Nano-PSiF the surface area was 68.4 m^2 g^{-1}.

Finally, electrochemical impedance spectroscopy was used to electrochemically characterize of Nano-PSiF and commercial silicon flour, by superposition of 5 mV sinusoidal potential on the midpoint potential of the anodic and cathodic cyclic voltammetric peaks of $[Fe(CN)_6]^{3-/4-}$, from 100 kHz to 0.1 Hz. The results indicate that the electrochemical impedance spectrum of Nano-PSiF-modified GCE is clearly different from that of the commercial silicon flour-modified GCE. Based on the results, the values of the charge transfer resistances (R_{ct}) were 5.2 and 20.8 KΩ for Nano-PSiF-modified GCE and commercial silicon flour-modified GCE, respectively. These results confirms that the conductivity of Nano-PSiF is higher (R_{ct} is lower) than the commercial silicon flour (results not shown).

After synthesis of the bimetallic silicon nanostructures, different methods including TEM, XPS, EDS, XRD and electrochemical methods were used to investigate the characteristics of Pt-M/PSiF (M: Pd, Rh, Ru). The compositions of Pt-M/PSiF were analyzed using EDS. The results are given in Table 1, clearly shows the presence of Si, Ag, Pt, Pd, Ru, Rh elements with their weights percent, weight ratio of the noble metals to silicon, and the ratio of the noble metals too (Pt/Pd, Pt/Ru, Pt/Rh). These results demonstrated that Pt-M/PSiF nanostructures were successfully synthesized. **"Here Table 1"**

The XRD patterns of Pt/PSiF (a), Pt-Pd/PSiF (b), Pt-Ru/PSiF (c), and Pt-Rh/PSiF (d) nanostructures are illustrated in Fig. 4A. For PSiF, six diffraction peaks at 2θ = 28.5º, 47.1º, 56.0º, 69.0º, 76.1º, 87.9 º and 94.4º for Si (221), Si (311), Si (400), Si (331), Si (422), and Si (511), respectively are detected. The diffraction peaks at 2θ = 39.9º, 46.4º, 67.7 º, 81.6 º are indexed as Pt/PtO_2 (111), (200), (220), (311) and (222), respectively those were observed for the bimetallic silicon nanostructures (Pt, Pt-Pd, Pt-Rh and Pt-Ru). In addition, the diffraction peaks at 2θ = 40.2º, 46.8º, 68.3 º, 82.3º and 86.8 º are indexed (111), (200), (220), (311) and (222), for Pd/PdO, 2θ = 38.4º (001), 42.2º (200), 44.0º (101), 58.3º (201), 69.4º (011), 78.4º (301), 82.2º (002), 84.7º (211), 86.0 (102), 92.0 (400), 97.1 (202) for Ru/RuO_x and 2θ = 41.0º (111), 47. 6º (002), 69.6º (022), 84.1º (113), 88.9º (222) for Rh must be observed, whereas in the mentioned 2θ non-index peaks intended because XRD cannot show the index peaks for the elements (Pd, Ru, Rh) at low weight percentages (lower than 5%, based on the results of EDS). However, change in the intensities of XRD, XPS and EDS peaks of Pt, confirming the formation of platinum-second metal (-palladium, -rhodium and/or -ruthenium).

XPS was applied to reveal the chemical composition of the metallic-silicon nanostructures. Figs. 4B, 4C and 4D show the XPS spectra of the Pt-Pd/PSiF and Pt/PSiF. The O1s spectra in Fig. 4B clearly indicates that there is a much higher contribution of oxygen in the porous silicon, Pt-Pd/PSiF. A feature related to the Si–O–Si caused by surface oxidation of PSiF and Pt-M/PSiF on air. Figs. 4C-a and 4C-b show Si (2p) peak of the silicon nanostructures of Pt/PSiF and Pt-Pd/PSiF, respectively. Here, Pt/PSiF shows spin-orbit coupled doublet (Si $2p^{3/2}$ and Si $2p^{1/2}$), whereas Pt-Pd/PSiF shows four peaks related to Pt and Pd at the surface of PSiF. Moreover, to confirm the synthesis of Pt-Pd/PSiF, XPS spectra of Pd/PSiF was also recorded (Fig. 4C-c). The results are as the same results as Pt and Pt-Pd silicon nanostructures, whereas Si (2p) spin-orbit coupled doublet (Si $2p^{3/2}$ and Si

$2p^{1/2}$) for Pd/PSiF has the binding energy lower than Si(2p) for Pt/PSiF. These results confirm the complete synthesis of Pt-Pd/PSiF. Combination of Pd-Pd on the surface of PSiF causes observing of four peaks for Si in Pt-Pd silicon nanostructure.

XPS spectra for Pt in Pt-Pd/PSiF for spin-orbit binding energy 4f are shown in Figs. 4D-a. The binding energies at 76 and 73 eV are corresponding to the spin–orbit split states of Pt, $4f^{5/2}$ and $4f^{7/2}$, respectively. Those binding energies were observed for both of Pt/PSiF and Pt-Pd/PSiF. According to the results, the binding energies of Pt and PtO_2 confirmed that 90% of the Pt on the surface of silicon is PtO_2. This investigation for Pt-Pd silicon nanostructure (according to Pt, $4f^{5/2}$ and $4f^{7/2}$) showed the same results as for the other synthetic bimetallic silicon nanostructures (Pt-Pd, Pt-Rh, Pt-Ru). Moreover, for Pt-Pd/PSiF in span of 315 to 340 eV (Fig. 4D-b) six peaks could be observed (including two peaks related to PtO_2 ($4d^{3/2}$ and $4d^{5/2}$ in 316 and 332 eV) and four peaks related to Pd and PdO ($3d^{3/2}$ and $3d^{5/2}$). Moreover, to confirm the synthesis of Pt-Pd/PSiF, XPS spectra of Pd/PSiF was also recorded and the results are shown in Fig. 4D-c. The results show as Pd silicon nanostructures in span of 315-340 with four peaks related to Pd and PdO spin-orbit coupled doublet. In addition, Rh specific peaks ($3d^{3/2}$ and $3d^{5/2}$ in 310 and 314 eV for Pt-Rh/PSiF) and Ru/RuO_x specific peaks ($3d^{3/2}$ and $3d^{5/2}$ in 284.4 and 281.1 eV for Pt-Ru/PSiF) could be observed too. It also indicated that Pt, Pt-Pd, Pt-Rh, and Pt-Ru nanoparticles were successfully synthesized on the PSiF surface.[42] **"Here Fig. 4"**

The morphologies and structures of the bimetallic silicon nanostructures were further investigated using TEM images. Pt-M silicon nanostructures morphologies were studied after chemical reduction of Pt-Pd, Pt-Ru and Pt-Rh from solution of K_2PtCl_6/K_2PdCl_4 and/or $RuCl_3.XH_2O$, and/or $RhCl_3.XH_2O$. The TEM images of Pt, Pt-Pd, Pt-Ru and Pt-Rh silicon nanostructures are shown in Figs. 5A and 5B (a-d). These images confirm that the bimetallic nanoparticles were growth on the surface of commercial silicon crystal (after etching) with

different orientations. The TEM images show a good dispersion of the nanoparticles on the PSiF surfaces for all of the investigated metal-modified silicon nanostructures.

"Here Fig. 5"

The electrochemical characterization of Pt-M/PSiF (M: Pd, Ru, Rh) nanostructures and combination of their nanostructures with reduce graphene oxide, as a catalyst on the surface of glassy carbon, were investigated in H_2SO_4. The modified electrodes were prepared using silicon nanostructure ink, by dispersion of 5.0 mg of the electrocatalysts (Pt/PSiF, Pt-Ru/PSiF, Pt-Rh/PSiF and Pt-Pd/PSiF) in 1.0 mL water under ultrasonic agitation for 20 min. Then, the metals modified silicon nanostructures ink (10 μL) was drop on the surface of a GCE or eRGO/GCE and they were dried at room temperature. Finally, 10 μL of Nafion solution (2.0%) was drop at the surface of Pt-M/PSiF and they were dried at room temperature. Then, cyclic voltammograms of the modified electrodes were recorded in 0.5 mol L^{-1} H_2SO_4 (Fig. 6). The cyclic voltammetric responses of Pt-M/PSiF–GCE (M: Pd, Ru, and Rh) are shown in Figs. 6A-a, 6B-a, and 6C-a. The cyclic voltammograms of Pt-M/PSiF–eRGO/GCE (M: Pd, Ru, and Rh) are also shown in Figs. 6A-b, 6B-b and 6C-b. It is clearly observed that the cathodic and anodic peaks current of Pt-M/PSiF–eRGO/GCE significantly are higher than Pt-M/PSiF–GCE. This process could be justified by increasing the specific surface area and excellent electrical conductivity of eRGO/GCE *vs.* GCE.

"Here Fig. 6"

One of important parameter can be obtained from the electrochemical study in performance of the noble metals in the silicon nanostructures is electrochemical active surface area (EAS) and catalytic activity. Cyclic voltammetry is a good method to determine EAS and the corresponding electrochemical activity of the bimetallic silicon nanostructures. The EASs were investigated using the cyclic voltammetric data recorded in the potential range of –0.30 V to 1.50 V *vs.* Ag/AgCl in 0.5 mol L^{-1} H_2SO_4 solution (saturated with high

purity nitrogen) at scan rate of 10 mV/s. As –0.20 V is a suitable applied potential for adsorption of hydrogen at the surface of Pt, this potential was selected to study the EAS of the bimetallic silicon nanostructures. Variations in the shape of the voltammograms suggest different catalytic facet exposure on the surface of the varying silicon nanostructures. The area of H-adsorption can be used to estimate the EAS of Pt catalysts,[37] according to the following equation:

$$EAS = (Q_H / 2.1\times 10^{-4})\ cm^2 \qquad (7)$$

Where, Q_H represents the charge-exchanged during the adsorption of hydrogen on the bimetallic silicon nanostructures surface and 2.1×10^{-4} C cm^{-2} is taken for the charge required to oxidize a monolayer of hydrogen on a smooth polycrystalline Pt electrode. The results showed higher EAS for the bimetallic silicon nanostructures compared to Pt/PSiF. Moreover, presence of graphene as a sub-layer of silicon nanostructures strongly increases the EAS of the silicon nanostructures. The result given in Table 2.

3.3. Electrocatalytic Activities of Nano-PSiF and the Bimetallic Silicon Nanostructures

First role of commercial silicon (110) and Nano-PSiF on the electrochemical HER was evaluated in acidic solution (H_2SO_4). The commercial silicon (110) or Nano-PSiF was dispersed in H_2O followed by dropping of the Nano-PSiF or silicon suspension onto a clean GCE surface or onto eRGO/GCE surface. Finally, 10 μL of Nafion solution (2.0%) was drop to the surface of the modified electrodes and allowed to dry at room temperature. Figure 7A shows the room temperature polarization data under acidic conditions for commercial silicon (110) and Nano-PSiF modified GCE. The results show that the over-potential for the electrochemical HER at Nano-PSiF is ~400 mV less than the commercial silicon. Nano-PSiF can accelerate the electrochemical hydrogen generation based on the following reasons: 1) when water molecules diffuse to a favorable dissociation site (Si in

nonporous surface) on the Nano-PSiF, its spontaneously split into two fragments bonded to two adjacent Si-H and Si-OH; 2) surface autocatalytic effect of Nano-PSiF reduces the activation barrier for segregation; 3) larger specific surface area of Nano-PSiF and consequently, the higher autocatalytic activity in HER; 4) finally, H_2O molecules adsorb and dissociate in this sustained dynamic process giving rise to efficient hydrogen generation. This study provides a molecular-level understanding of the hydrogen generation mechanism and reveals that Nano-PSiF with surface autocatalytic effects can be used to split water with high efficiency, by enabling renewable and economical generation of hydrogen.[29, 30]

The activities of the bimetallic silicon nanostructures for HER were evaluated in acidic conditions by dispersing the Pt-M silicon nanostructures in H_2O followed by dropping the bimetallic silicon nanostructures at the surface of a clean GCE or at eRGO/GCE. Figure 7B shows the room temperature polarization data under acidic conditions for various catalysts, including films of Pt/PSiF, Pt-Pd/PSiF, Pt-Rh/PSiF and Pt-Ru/PSiF on GCE and on eRGO/GCE. The results for Pt/PSiF nanostructure showed that an overpotential (η) less than 100 mV was required to sustain the cathodic current density in excess of 10 mA cm^{-2}, and this is comparable with commercial Pt/C. This activity greatly exceeded due to the presence of Nano-PSiF at the surface of GCE. After addition of the second metal (Pd, Rh, Ru) beside of Pt, the current densities and the overpotentials were reduced too. To investigate the promotional effect of the different metals (Pd, Rh, Ru) on the electrocatalytic activity of modified silicon nanostructure in HER, i–E curves were recorded at 0.0 to –0.30 V in 0.5 mol L^{-1} H_2SO_4. Fig. 7B show overpotential for HER at Pt/PSiF and Pt-M/PSiF (M: Ru, Rh, Pd) at current density of 10 mA cm^{-2}. The results confirm that Ru, Rh and Pd act as effective promoters, whereas the best promoter was Pd. On the other hand, Rh and Ru give lower promotion effect to the activity of Pt/PSiF than Pd. Although Pd, Ru and Rh have electrocatalytic properties for HER, but their electrocatalytic effects are lower than Pt.

When Pt makes a bimetallic alloy with Pd, or Ru and/or Rh, the other factors such as real surface area could be affect the electrocatalytic behavior. For this purpose, the roughness factors of the Pt-M/PSiF-GCE and Pt/PSiF–GCE were determined by ratio of the real surface area to the geometric surface area. The real surface areas of Pt-M/PSiF-GCE and Pt/PSiF–GCE were estimated by a calculation of the hydrogen adsorption/desorption area in the cyclic voltammograms in acidic media. The results of the roughness factor ratio are given in Table 2A.

The role of reduce graphene oxide, as a sub-layered for the bimetallic silicon nanostructures on HER, was investigated too. The highest electrocatalytic activities (for Pt/PSiF, Pt-Pd/PSiF, Pt-Rh/PSiF and Pt-Ru/PSiF) were observed after electrodeposition of reduce graphene oxide at the surface of GCE. As shown in Fig. 7C, combination of the bimetallic silicon nanostructures and reduce graphene oxide cause increasing the current densities and decreasing the over-potentials of the electrocatalysts for HER. This process can be attributed to increasing of the specific surface area and excellent conductivity of reduce graphene oxide on the silicon nanostructures, as shown in Fig. 2D. The surface area of the electrocatalysts, after immobilization of silicon nanostructure at the surface of eRGO/GCE, were measured by hydrogen adsorption/desorption area and then the roughness factors ratio were determined (Table 2B). The results are comprised with the real surface area of the modified-silicon nanostructures (that immobilize on the surface of GCE). Finally, present of reduced graphene oxide increases the electrocatalytic activity of the modified silicon nanostructures for HER. **“Here Table 2” “Here Fig. 7”**

One of the important issues (than the high activity) is the stability of an electrocatalyst. To assess this, long term durability were tested to demonstrate the thermodynamic stability of Nano-PSiF and the bimetallic silicon nanostructures. In the case of Nano-PSiF, its activity after 500 consecutive cycles is quite similar to the initial one but

the current density reduces and onset potential increases. This is due to the surface coverage of Nano-PSiF by hydrogen.[30] High durability of the bimetallic silicon nanostructures were also investigated using 500 consecutive cycles (~12 h) using cyclic voltammetry. At the end of cycling, the catalysts afforded similar i–E curves as before, with negligible loss of the cathodic currents (Figs. 8A and 8B). **"Here Fig. 8"**

3.4. Tafel Analysis and HER Mechanism Silicon Nanostructure

Tafel analysis was carried out on the polarization curves of Nano-PSiF, Pt/PSiF and Pt–M/PSiF nanostructures in 0.5 mol L^{-1} H_2SO_4. The results are summarized in Table 3. The Tafel slopes for the bimetallic silicon nanostructures were found to be between 39–43 mV $dec^{-1.}$ Tafel slope for Nano-PSiF was determined as 184.2 mV dec^{-1}. The best three promoters, Pd, Ru and Rh, significantly increased the exchange current densities (J_0). The Pd–Pt silicon nanostructure has the highest J_0, which is a 4-fold of Pt silicon nanostructure.

In acidic solutions, HER on a metal surface mainly involves three reactions (Eq. 8–10). The common first step is the discharge reaction or Volmer step (8), which is followed by either Tafel step (9) or Heyrovsky step (10) to give H_2. Tafel analysis has been used to distinguish different mechanistic pathways. Assuming a small surface coverage of hydrogen, a fast discharge reaction (8) followed by a rate-determining combination reaction (9) results in a theoretical Tafel slope of 29 mV dec^{-1} at 25 ^{o}C (2.303RT/αF). This value was found experimentally for Pt. If reaction (8) is rate determining or the surface coverage is close to one, the Tafel slope should be 116 mV dec^{-1}.

Discharge reaction (Volmer step) is:

$$H_3O^+ + e^- + Cat \longrightarrow Cat\text{–}H + H_2O \qquad b=2.3RT/\alpha F = 120 \text{ mV dec}^{-1} \text{ (if } \alpha=0.5) \quad (8)$$

Combination reaction (Tafel step) is:

$$\text{Cat–H} + \text{Cat–H} \longrightarrow 2\text{Cat} + H_2 \qquad b = 40\ \text{mV dec}^{-1}\ (\text{if } \alpha = 0.5) \qquad (9)$$

Ion + atom reaction (Heyrovsky step):

$$H_3O^+ + e^- + \text{Cat–H} \longrightarrow \text{Cat} + H_2 + H_2O \qquad b = 30\ \text{mV dec}^{-1}\ (\text{if } \alpha = 0.5) \qquad (10)$$

However, deviation from these values are also common. Many factors may be the origins for the deviation. The surface coverage of hydrogen might be intermediate and potential dependent, or the discharge reaction may have a significant activation barrier. [43, 44]

The correlation between the Tafel slopes and the mechanism of HER was developed for metal surfaces, on which the Volmer step could be observed by cyclic voltammetry. The Nano-PSiF catalyst is non-metallic, and the Volmer step is not observed by cyclic voltammetry, whereas for the bimetallic silicon nanostructures Volmer step can be observed. However, Tafel analysis is still a useful tool here, because the experimentally observed Tafel slopes indeed approach a limiting value of 38 mV dec^{-1}. Following these considerations, HER catalyzed by Nano-PSiF in acidic solution seems to occur via a fast discharge reaction and then a rate-determining discharge reaction. A slightly higher Tafel slope was observed for Nano-PSiF. This is probably due to a variation in the surface coverage of hydrogen rather than a different mechanistic pathway.

The observed Tafel slope for Pt-PSiF nanostructure (46.9 mV dec^{-1}) in the current work was lower than of Pt-Ru/PSiF and Pt-Ru/PSiF (51.4, 47. mV dec^{-1} for Pt-Rh and Pt-Ru, respectively) and was higher than Pt-Pd/PSiF, whereas for all of the electrocatalysts, the Tafel slopes were near to 40. As a result, suggesting that the electrochemical desorption is the rate-determining step or the Volmer-Heyrovsky mechanism (Eqs. 6 and 8) is operative in the HER catalyzed by the bimetallic silicon nanostructures. This means that when a

combination of silicon nanostructures and reduce graphene oxide was used, the Tafel slope reduced to 39.6 mV dec^{-1} for Pt-Pd/PSiF–eRGO/GCE and the kinetic of the reaction increases, while HER mechanism does not change.[38] The other kinetic parameters such as Tafel equation and nα are also given in Table 3, those confirm the fast kinetic for HER.

"Here Table 3"

3.5. Electrochemical Impedance Spectroscopy

Electrochemical impedance spectroscopy (EIS) was used to study Nano-PSiF and the Pt-M/PSiF nanostructures for the electrochemical HER. Fig. 9A shows the electrochemical impedance spectra of Nano-PSiF and/or PSiF drop-cast on a surface of GCE, those were achieved at a potential of –400 mV (*vs.* Ag/AgCl) in 0.5 mol L^{-1} H_2SO_4. The results showed that the charge transfer resistance (from Nyquist plots) of the GCE reduced greatly after the drop-casting of the commercial silicon or Nano-PSiF. Moreover, charge transfer resistance of Nano-PSiF was much smaller than for commercial silicon in electrochemical HER. Thus, we presume that formation of nano-porous holes on the surface of silicon flour increase the electrical conductivity and improve the electrochemical activity for HER.

Nyquist plots of Pt-M/PSiF (M: Ru, Rh, Pd) at GCEs were achieved at a potential of –250 mV (*vs.* Ag/AgCl) in 0.5 mol L^{-1} H_2SO_4 too. All Nyquist plots of Pt-M/PSiF exhibit two semicircles; first semicircle diameter is independent to the applied potential, this resistances is related to silicon nanostructure tangles/laminated or adsorption/desorption of H_2 at the surface of the silicon nanostructure. The second semicircle diameter corresponds to constant charge transfer resistance (R_{ct}) for HER. It can be seen that the sequence of the values of R_{ct} for the different modified-GCEs is: Pt-Pd/PSiF < Pt-Rh/PSiF < Pt-Ru/Psi < Pt/PSiF (Figs. 9B, and 9C).

To consider the electron transfer kinetics of HER, the impedance of Pt-M/PSiF-GCE at various over-potentials were recorded in 0.5 mol L^{-1} H_2SO_4. For example, Figs. 9B shows

the Nyquist plots of the EIS responses of Pt-Pd/PSiF–eRGO/GCE. The results of the Nyquist plots demonstrated two semicircles; first semicircle diameter is independent to the applied potential, whereas the second semicircle indicating charge transfer resistance for HER, is characterized by one times constant. The charge transfer resistance R_{ct} is related to the kinetics of the electrocatalyst, and a lower value corresponds to a faster reaction rate. As expected, this resistance is overpotential independent, whereas the R_{ct} depends strongly on the overpotentials. Moreover, Bode plots showed that the phase angle is depends on the frequency. This result suggests an additional resistor element in the series with the above-mentioned two elements. The similarity among the response of all films suggests a similar mechanism for electrochemical HER. [44–48] **"Here Fig. 9"**

4. Conclusion

Efficient electrochemical HER through electrocatalyst at low overpotentials holds tremendous promise for clean energy. Silicon nanostructure is a suitable photochemical catalyst in water splitting. Silicon nanostructure is also suitable in electrochemical HER. The electrocatalytic activity of silicon nanostructure is due to spontaneously dissociate of water via a surface autocatalytic process forming a complex consisting of –H and −OH fragments, whereas water molecules could not adsorb onto the surfaces of silicon nanostructure. This arises from the large reduction in the activation barrier on the silicon nanostructure enabling efficient dissociation of H_2O molecules. Here, bimetallic silicon nanostructures of the noble metals (Pt group: Pt, Pd, Rh and Ru) were synthesized via a facile galvanic replacement. Then, the electrocatalytic activities of those nanocomposites for HER were investigated. The nanocomposites showed good electrochemical activity for HER in comparison with commercial Pt/C. In addition, the key challenges for even of the electrocatalysts are increasing the number of catalytic active sites and suitable electrical conductivity. For this

purpose, reduced graphene oxide was deposited on the surface of GCE, because eRGO/GCE has higher surface area and higher electrical conductivity in comparison with GCE. Finally, the properties of the hybrid bimetallic silicon nanostructures on RGO-GCE (Pt-M/PSiF–eRGO) in HER activity were investigated. The results confirmed that Pt-M/PSiF–eRGOs have higher electrocatalytic activates for HER, with a small overpotentials of ~0.02–0.05 V, large cathodic currents and Tafel slopes as small as 39.6 mV decade^{-1}.

Acknowledgements

The authors wish to thank the Iran National Science Foundation and National Elites Foundation, for their support.

References

1 S. Fukuzumi, Y. Yamada, T. Suenobu, K. Ohkubo, H. Kotani, *Energy Environ. Sci*., 2011, **4**, 2754.

2 S. Fukuzumi, Y. Yamada, *J. Mater. Chem*. 2012, **22**, 24284.

3 T. A. Faunce, W. Lubitz, A. W. B. Rutherford, D. MacFarlane,G. F. Moore, P. Yang, D. G. Nocera, T. A. Moore, D. H. Gregory, S. Fukuzumi, *Energy Environ. Sci*. 2013, **6**, 695.

4Y. Tachibana, L. Vayssieres, J. R. Durrant, *Nat. Photonics*, 2012, **6**, 511.

5 Ch. Tsai, K. Chan, J. K. Nørskov, F. Abild-Pedersen, *Catal. Sci. Technol*. 2015, **5**, 246.

6 Y. Yamada, S. Shikano, S. Fukuzumi, *J. Phys. Chem. C*, 2013,**117**, 13143.

7 D. G. Nocera, *Chem. Soc. Rev*. 2009, **38**, 13.

8 P. D. Tran, S. S. Pramana, V. S. Kale, M. Nguyen, S. Y. Chiam, S. K. Batabyal, L. H. Wong, J. Barber, J. Loo, *Chem. Eur. J.* 2012, **18**, 13994.

9 M. D. Kärkäs, O. Verho, E. V. Johnston, B. Åkermark, *Chem. Rev.* 2014, **114**, 11863.

10 J. Zhang, Y. Wang, J. Zhang, Z. Lin, F. Huang, J. Yu, *ACS Appl. Mater. Inter.* 2013, **5**, 1031.

11 P. Jiang, Q. Liu, C. Ge, W. Cui, Z. Pu, A. M. Asirib, X. Sun, *J. Mater. Chem. A*, 2014, **2**, 14634.

12 J. Maruyama, T. Ioroi, Z. Siroma, T. Hasegawa, A. Mineshige, *ChemCatChem,* 2013, **5**, 130.

13 I. L. C. Buurmans, J. R. Martínez, W. V Knowles, D. Beek, J. A. Bergwerff, *Nature Chem*. 2011, **3**, 862.

14 X. S. Zhou, Z. R. Dong, H. M. Zhang, J. W. Yan, J. X. Gao, B. W. Mao, *Langmuir,* 2007, **23**, 6819.

15 S. Trasatti, O. A. Petri, *Pure. Appl. Chem.* 1991, **63,** 711.

16 T. R. Cook, D. K. Dogutan, S. Y. Reece, Y. Surendranath, T. S. Teets, D. G. Nocera, *Chem. Rev*. 2010, **110**, 6474.

17 M. Gratzel, *Nature,* 2001, **414**, 338.

18 M. G. Walter, E. L. Warren, J. R. Mckone, S. W. Boettcher, Q. X. Mi, E. A. Santori, N. S. Lewis, *Chem. Rev*. 2010, **110**, 6446.

19 X. Cx, L. Wang, R. Y. Wang, K. Wang, Y. Zhang, F. Tian, *Adv. Mater.,* 2009, **21**, 2165.

20 E. S. Andreiadis, P. Jacques, A. P. D. Tran, A. Leyris, M. C. Kerlidou, B. Jousselme, M. Matheron, J. Pécaut, S. Palacin, M. Fontecave, V. Artero, *Nature Chem.* 2013, **5**, 48.

21 Y H. Lai, H. S. Park, J. Z. Zhang, P. D. Matthews, D. S. Wright, E. Reisner, *Chem. Eur. J.* 2015, **21**, 3919.

22W. F. Chen, K. Sasaki, C. Ma, A. I. Frenkel, N. Marinkovic, J. T. Muckerman, Y. Zhu, R. R. Adzic, *Angew. Chem., Int. Ed*., 2012, **51**, 6131.

23 L. A. Kibler, *Chem. Phys. Chem.,* 2006, **7**, 985.

24 L. A. Kibler, A. M. El-Aziz, R. D. Hoyer, D. M. Kolb, *Angew. Chem., Int. Ed.,* 2005, **44,** 2080.

25 J. Greeley, J. K. Nørskov, L. A. Kibler, A. M. El-Aziz, D. M. Kolb, *Chem. Phys. Chem.,* 2006, **7**, 1032.

26 C. L. Green, A. Kucernak, *J. Phys. Chem. B,* 2002, **106**, 1036.

27 A. A. Ensafi, M. Jafari-Asl, B. Rezaei, *J. Electroanal. Chem.,* 2014, **731**, 20.

28 A. A. Ensafi, M. Jafari-Asl, B. Rezaei, *Electrochim. Acta,* 2014, **130**, 397.

29 Ch. He, X. Wu, J. Shen, P. K. Chu, *Nano Lett.* 2012, **12**, 1545.

30 X. L.Wu, S. J. Xiong, J. Zhu, J. Wang, J. C. Shen, P. K. Chu*, Nano Lett.* **2009**, 9, 4053.

31 Y. Yan, L. Zhang, X. Qi, H. Song, J. W. Wang, H. Zhang, X. Wang, *Small*, 2012, **8**, 3350.

32 J. Huang, Y. Wu, D. Wang, Y. Ma, Z. Yue, Y. Lu, M. Zhang, Z. Zhang, P. Yang, *ACS Appl. Mater. Inter.* **2015**, 7, 3732-3741.

33 Z. Huang, Ch. Wang, Zh. Chen, H. Meng, C. Lv, Z. Chen, R. Han, Ch. Zhang, *ACS Appl. Mater. Inter.* **2014**, 6, 10408–10414.

34 A. A. Ensafi, M. Jafari-Asl, B. Rezaei, *Talanta,* 2013, **103**, 322.

35 H. L. Guo, X. F. Wang, Q. Y. Qian, F. B. Wang, X. H. Xia, *ACS Nano*, 2009, **3,** 2653.

36 T. Nakamura, S. Adachi, *J. Luminescence,* 2012*,* **13**, 3019.

37 A. A. Ensafi, M. Jafari-Asl, B. Rezaei, M. Mokhtari Abarghoui, H. Farrokhpour, *J. Power Sources*, 2015, **282**, 452.

38 H. Ji, M. Li, Y. Wang, F. Gao, *Electrochem. Comm.* 2012, **24**, 17.

39 A. J. Uhlir, Bell Syst, *Technol. J.* **1956**, 35, 333.

40 Y.H. Ogata, T. Tsuboi, T. Sakka, S. Naito, *J. Porous Mater*, 2000, **7**, 63.

41 L. T. Canham, *Appl. Phys. Lett.* 1990, **57**, 1046.

42 J. N. Tiwari, R. N. Tiwari, L. K. Lin, *Appl. Mater. Inter.* 2010, **2**, 2231-2237.

43 Y. Li,Y. H. Wang, L. Xie, Y. Liang, G. Hong, H. Dai, *J. Am. Chem. Soc.,* 2011, **133**, 7296.

44 Y. H. Chang, C. T. Lin, T. Y. Chen, C. L. Hsu, Y. H. Lee, W. Zhang, K. H. Wei, L. Li, *J. Adv. Mater*. **2013**, 25, 756.

45 T. Wang, L. Liu, Z. Zhu, P. Papakonstantinou, J. Hu, H. Liu, M. Li, *Energy Environ. Sci*. 2013, **6**, 625.

46 Y. Yan, B. Xia, X. Qi, H. Wang, R. Xu, J. Y. Wang, H. Zhang, X. Wang, *Chem. Commun.* 2013, **49**, 4884.

47 M. Nguyen, P. D. Tran, S. S. Pramana, R. L. Lee, S. K. Batabyal, N. Mathews, L. H. Wong, M. Graetzel, *Nanoscale,* 2013, **5**, 1479.

48 A. B. Laursen, S. Kegnaes, S. Dahl, I. Chorkendorff, *Energy Environ. Sci.*, 2012, **5**, 5577.

Legends for the figures:

Fig. 1. A): TEM of EGO; B): EDS results of EGO; C): Cyclic voltammograms of the electroreduction of exfoliate graphene oxide in carbonate buffer (pH 9.2) at a scan rate of 25 mV s^{-1}.

Fig. 2. A): Cyclic voltammograms of GCE (a), and eRGO/GCE (b) in 5.0 mmol L^{-1} $Fe(CN)_6^{3-/4-}$ solution containing 0.10 mol L^{-1} KNO_3. B): Nyquist plots for GCE (a), and eRGO/GCE (b) in $Fe(CN)_6^{3-/4-}$ solution (5.0 mmol L^{-1}) containing 0.10 mol L^{-1} KNO_3. C): FT–IR spectra of (a): EGO and (b): eRGO. D): Raman spectra of (a): EGO and (b): eRGO. E): FE-SEM images of eRGO/GCE.

Fig. 3. A): FE-SEM of Ag/PSiF; B): TEM images of Nano-PSiF, C) FT–IR of Nano-PSiF. D): High resolution XPS of (a) commercial silicon flour and (b) nano-porous silicon flour plus the curves fitting.

Fig. 4. A): XRD pattern of (a): Pt, (b): Pt-Pd, (c): Pt-Rh, and (d): Pt-Ru silicon nanostructures. B): Survey XPS data for (a) PSiF, (b) Pt-Pd/PSiF, C): High resolution XPS for Si element in (a): Pt/PSiF, (b): Pt-Pd/PSiF, and (c): Pd/PSiF plus the curves fitting. D): High resolution XPS of (a): Pt(4f) in Pt/PSiF, (b): Pt(4d) and Pd(3d) in Pt-Pd/PSiF, and (c): Pd(3d) in Pd/PSiF plus the curves fitting.

Fig. 5. A): and B): TEM images of a): Pt/PSiF; b): Pt-Pd/PSiF; c): Pt-Rh/PSiF; and d): Pt-Ru/PSiF with different magnitudes.

Fig. 6. Cyclic voltammograms of A): Pt-Pd/PSiF; B): Pt-Rh/PSiF; and C): Pt-Ru/PSiF at the surface of (a): eRGO/GCE, and (b): Unmodified-GCE, in 0.5 mol L^{-1} H_2SO_4 solution with scan rate of 50 mV s^{-1}.

Fig. 7. A): Liner sweep voltammograms for HER in 0.5 mol L^{-1} H_2SO_4 at (a): commercial silicon flour; (b): Nano-PSiF; (c): commercial Pt/C; those immobilized at the surface of GCE; B): Liner sweep voltammograms for HER in 0.5 mol L^{-1} H_2SO_4 at (a): Pt/PSiF; (b): commercial Pt/C; (c) Pt-Ru/PSiF; (d): Pt-Rh/PSiF; and (e): Pt-Pd/PSiF; those immobilize at the surface of eRGO/GCE. C): Liner sweep voltammograms for electrochemical HER in 0.5 mol L^{-1} H_2SO_4 at (a): Pt-Pd/PSiF-GCE; and (b): Pt-Pd/PSiF-eRGO/GCE; with a scan rate of 10 mV s^{-1}.

Fig. 8. Long-term electrochemical stability test in 0.5 mol L^{-1} H_2SO_4 at A): Nano-PSiF eRGO/GCE, and B): Pt-Pd/PSiF-eRGO/GCE, (a): first cycle, and (b): after 500 cycles; with a scan rate of 10 mV s^{-1}.

Fig. 9. A): Nyquist plots of a solution containing 0.5 mol L^{-1} H_2SO_4 at (a): commercial silicon flour modified GCE; (b): Nano-PSiF modified GCE at potential of -400 mV *vs.* Ag/AgCl. B): Nyquist plots of a solution containing 0.5 mol L^{-1} H_2SO_4 at (a): Pt/PSiF-GCE; (b): Pt-Ru/PSiF-GCE; (c): Pt-Rh/PSiF-GCE; and (d): Pt-Pd/PSiF-GCE at potential of -250 mV *vs.* Ag/AgCl. C): Nyquist plots of a solution containing 0.5 mol L^{-1} H_2SO_4 at (a): Pt-Pd/PSiF-GCE; (b): Pt-Pd/PSiF-eRGO/GCE. (D) Nyquist plots of a solution containing 0.5 mol L^{-1} H_2SO_4 at Pt-Pd/ PSiF-GCE in different potential of (–200, –220, –240, –260, –270, –280, –290, –300, –350 mV) *vs.* Ag/AgCl in 0.5 mol L^{-1} H_2SO_4.

Table 1. EDS results of the bimetallic silicon nanostructures.

Element.	Line	Intensity (c/s)	Atomic (%)	Concentration (wt.%)	
Si	Ka	2561.67	98.79	92.54	
Ag	La	18.52	1.21	7.46	
			100.00	100.00	Total
Si	Ka	2558.99	97.04	85.50	
Pt	La	20.32	2.96	14.50	
			100.00	100.00	Total
Si	Ka	3221.79	97.90	84.42	
Pd	La	17.83	0.96	5.32	
Pt	La	9.42	1.14	9.26	
			100.00	100.00	Total
Si	Ka	2130.039	97.12	86.00	
Ru	La	15.33	1.26	4.02	
Pt	La	9.07	1.62	9.98	
			100	100	Total
Si	Ka	2705.58	96.82	85.45	
Rh	La	27.24	1.7	5.51	
Pt	La	10.58	1.47	9.04	
			100	100	Total

Table 2A. Effect of the second metal on the roughness factor of the silicon nanostructures.

	Pt-Ru/PSiF	Pt-Rh/PSiF	Pt-Pd/PSiF	Pt /PSiF
Q_H(eRGO/GCE)	325.6	294.8	474	103
Q_H (GCE)	84	73.5	98.6	25.3
Roughness Factor Ratio (eRGO/GCE)	3.2	2.86	4.6	
Roughness Factor Ratio (GCE)	3.3	2.9	3.82	

Table 2B. Effect of eRGO on the roughness factor of the silicon nanostructures.

	Pt-Ru/PSiF	Pt-Rh/PSiF	Pt-Pd/PSiF	Pt /PSiF
Q_H (eRGO/GCE)	325.6	294.8	474	103
Q_H (GCE)	84	73.5	98.6	25.3
Roughness Factor Ratio	3.88	4	4.81	4.07

Table 3. Kinetic parameters of the silicon nanostructures.

	nα	OCP (*vs.* Ag/AgCl)	(Tafel slope)$^{-1}$	Tafel equation
Nano-PSiF	0.32	–0.450	184.2	y = –6.3x – 2.08
Pt/PSiF	1.25	–0.262	46.9	y = –21.2x – 4.2
Pt-Pd/PSiF	1.40	–0.225	41.9	y = –23.69x – 4.03
Pt-Pd/PSiF-eRGO	1.48	–0.213	39.6	y = –25.42x – 4.23
Pt-Rh/PSiF	1.14	–0.232	51.4	y = –19.34 – 4.25
Pt-Ru/PSiF	1.24	–0.230	47.5	y = –20.94x – 4.22

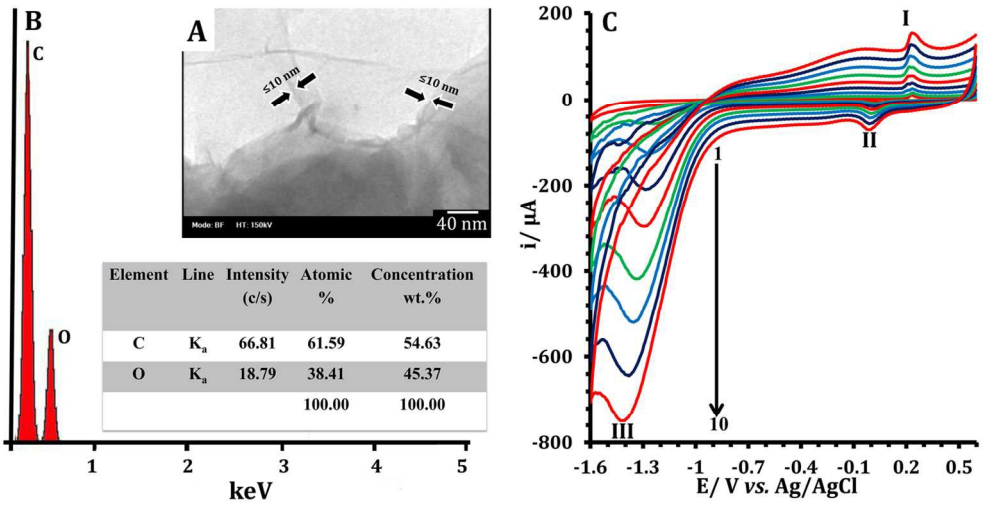

Element	Line	Intensity (c/s)	Atomic %	Concentration wt.%
C	K_a	66.81	61.59	54.63
O	K_a	18.79	38.41	45.37
			100.00	100.00

Fig. 1. A): TEM of EGO; B): EDS results of EGO; C): Cyclic voltammograms of the electroreduction of exfoliate graphene oxide in carbonate buffer (pH 9.2) at a scan rate of 25 mV s–1.
207x107mm (200 x 200 DPI)

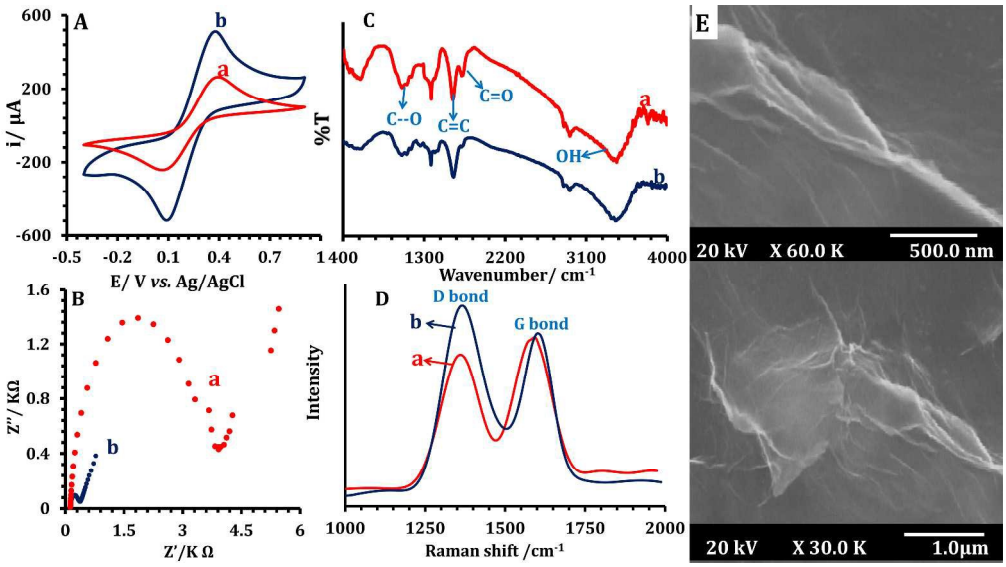

Fig. 2. A): Cyclic voltammograms of GCE (a), and eRGO/GCE (b) in 5.0 mmol L–1 Fe(CN)63–/4– solution containing 0.10 mol L–1 KNO3. B): Nyquist plots for GCE (a), and eRGO/GCE (b) in Fe(CN)63–/4– solution (5.0 mmol L–1) containing 0.10 mol L–1 KNO3. C): FT–IR spectra of (a): EGO and (b): eRGO. D): Raman spectra of (a): EGO and (b): eRGO. E): FE-SEM images of eRGO/GCE.
414x230mm (300 x 300 DPI)

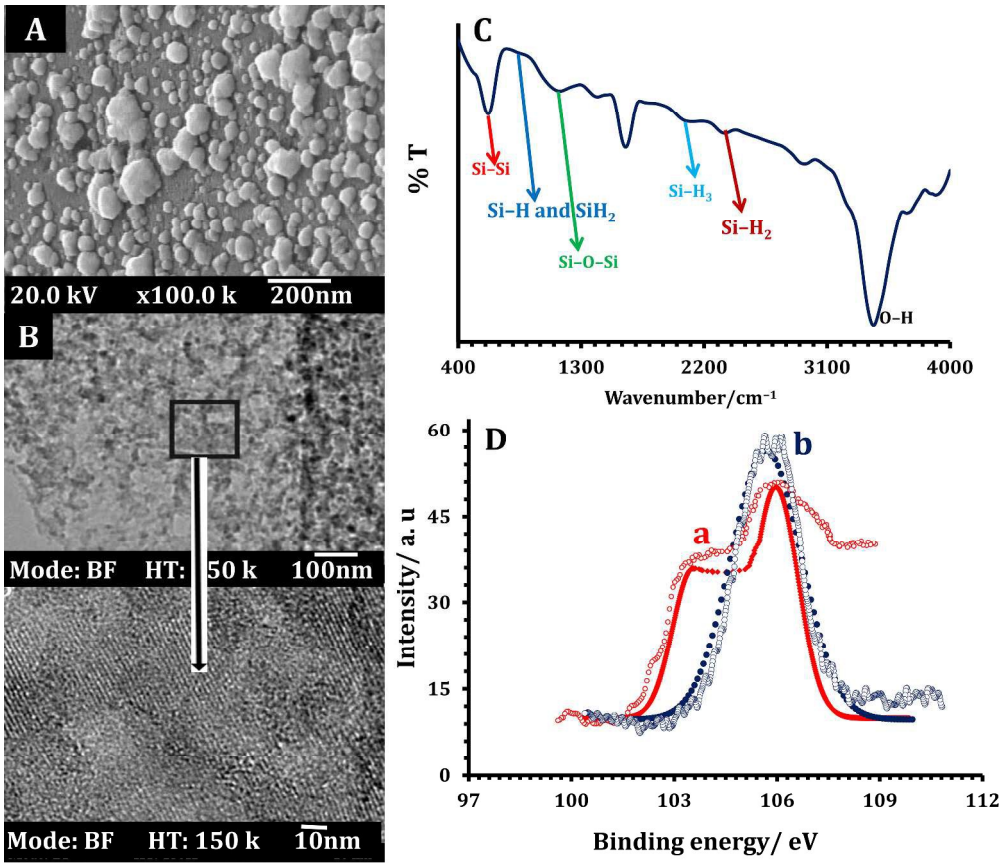

Fig. 3. A): FE-SEM of Ag/PSiF; B): TEM images of Nano-PSiF, C) FT–IR of Nano-PSiF. D): High resolution XPS of (a) commercial silicon flour and (b) nano-porous silicon flour plus the curves fitting.
351x300mm (300 x 300 DPI)

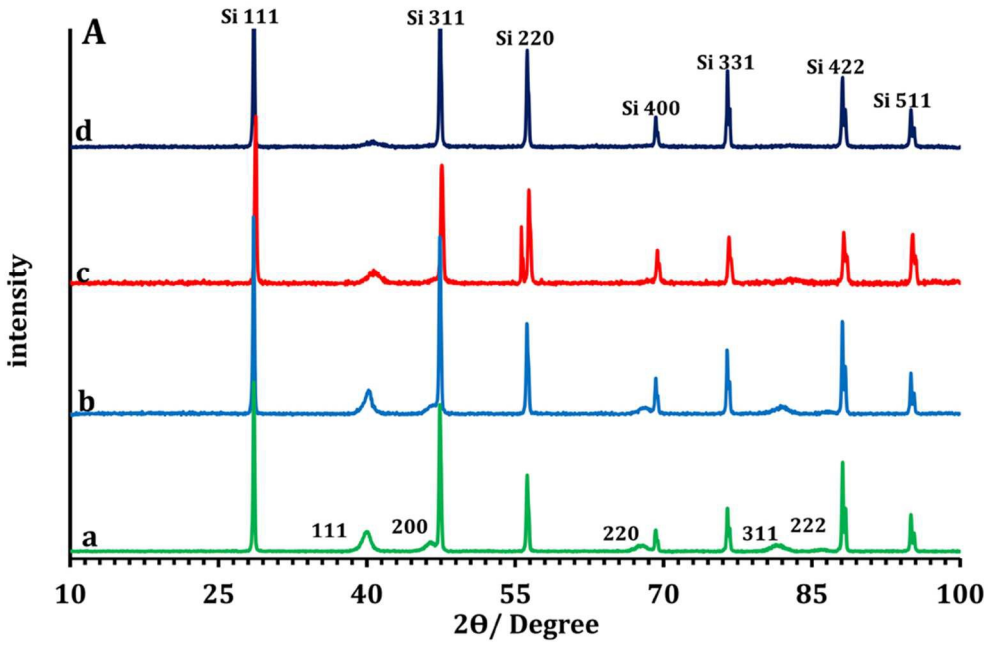

Fig. 4A. XRD pattern of (a): Pt, (b): Pt-Pd, (c): Pt-Rh, and (d): Pt-Ru silicon nanostructures.
261x174mm (100 x 100 DPI)

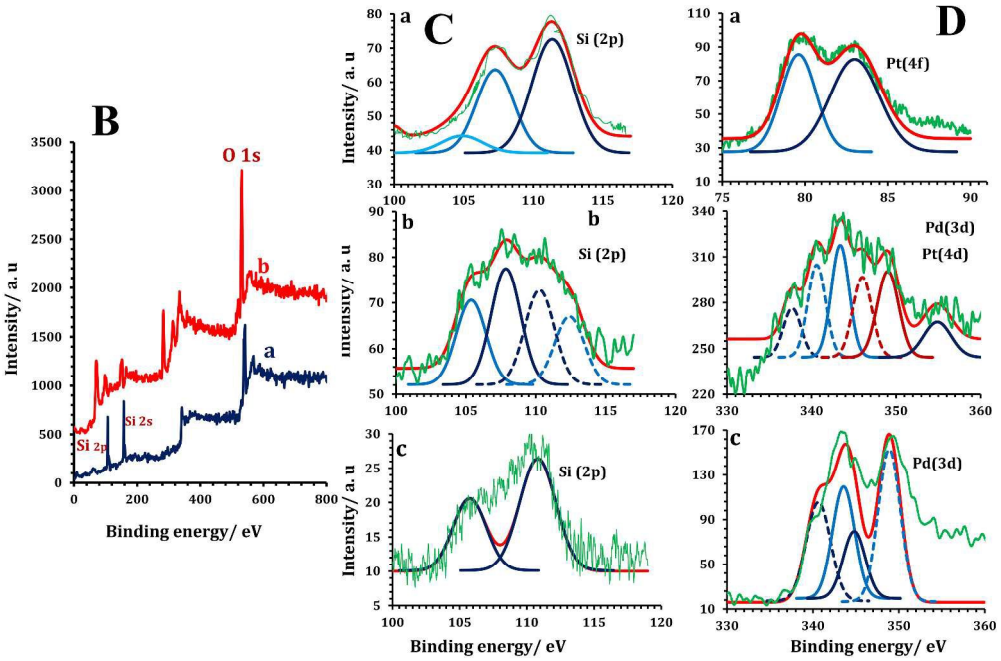

Figure 4: B): Survey XPS data for (a) PSiF, (b) Pt-Pd/PSiF, C): High resolution XPS for Si element in (a): Pt/PSiF, (b): Pt-Pd/PSiF, and (c): Pd/PSiF plus the curves fitting. D): High resolution XPS of (a): Pt(4f) in Pt/PSiF, (b): Pt(4d) and Pd(3d) in Pt-Pd/PSiF, and (c): Pd(3d) in Pd/PSiF plus the curves fitting.
465x306mm (300 x 300 DPI)

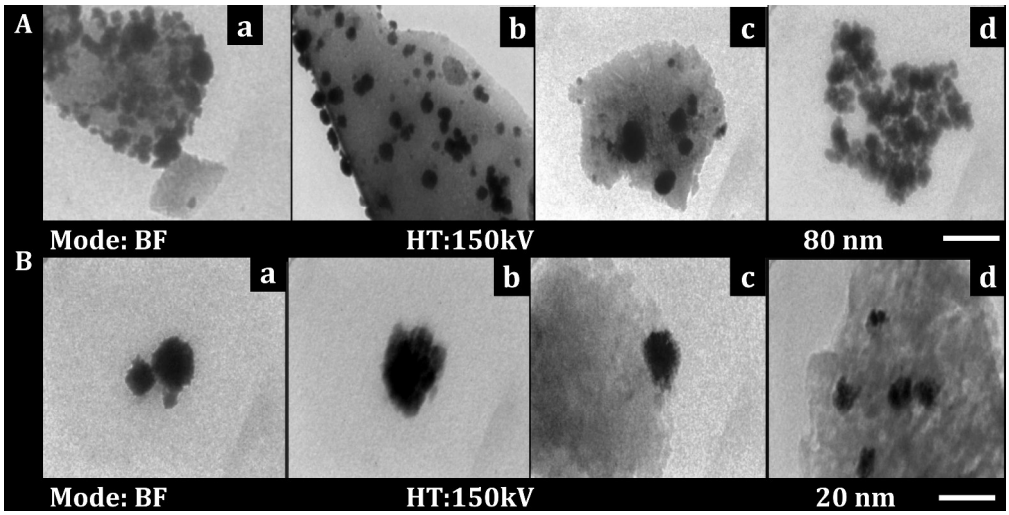

Fig. 5. A): and B): TEM images of a): Pt/PSiF; b): Pt-Pd/PSiF; c): Pt-Rh/PSiF; and d): Pt-Ru/PSiF with different magnitudes.
401x202mm (300 x 300 DPI)

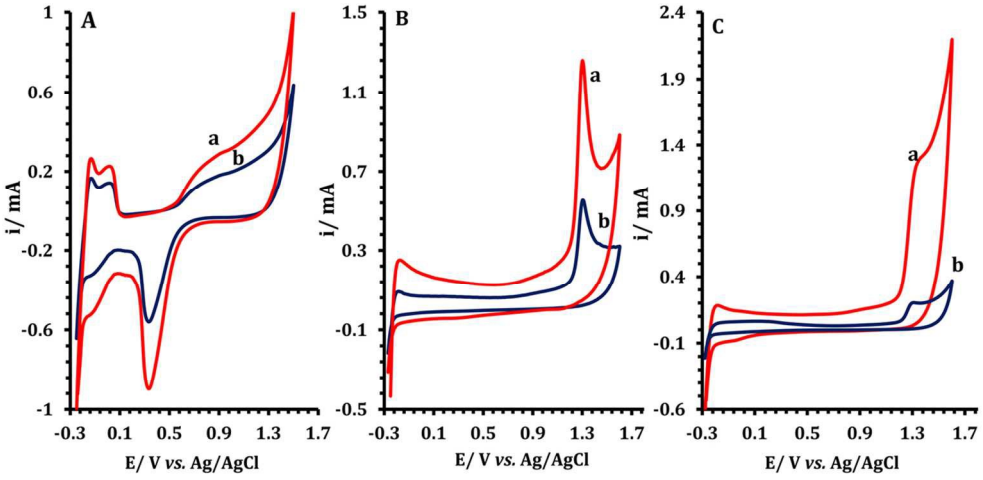

Fig. 6. Cyclic voltammograms of A): Pt-Pd/PSiF; B): Pt-Rh/PSiF; and C): Pt-Ru/PSiF at the surface of (a): eRGO/GCE, and (b): Unmodified-GCE, in 0.5 mol L–1 H2SO4 solution with scan rate of 50 mV s–1.
333x158mm (100 x 100 DPI)

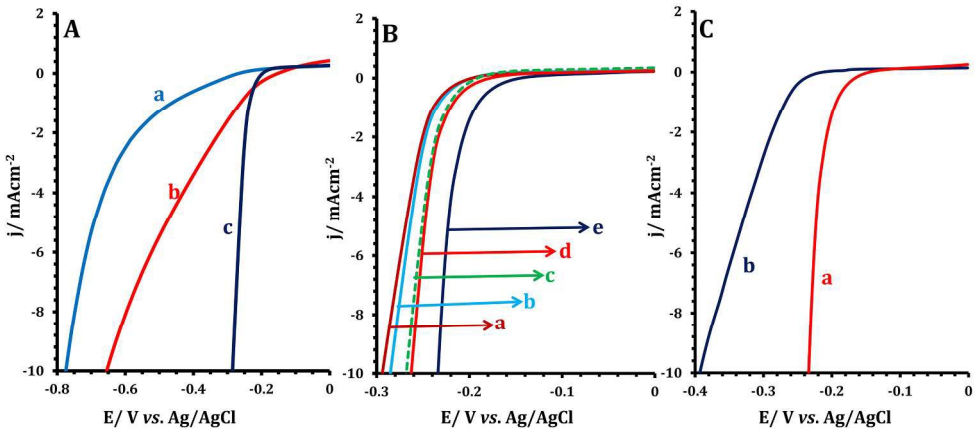

Fig. 7. A): Liner sweep voltammograms for hydrogen generation reaction in 0.5 mol L–1 H2SO4 at (a): commercial silicon powder; (b): Nano-PSiF; (c): commercial Pt/C; those immobilized at the surface of GCE; B): Liner sweep voltammograms for hydrogen generation reaction in 0.5 mol L–1 H2SO4 at (a): Pt/PSiF; (b): commercial Pt/C; (c) Pt-Ru/PSiF; (d): Pt-Rh/PSiF; and (e): Pt-Pd/PSiF; those immobilize at the surface of eRGO/GCE. C): Liner sweep voltammograms for electrochemical hydrogen generation in 0.5 mol L–1 H2SO4 at (a): Pt-Pd/PSiF-GCE; and (b): Pt-Pd/PSiF-eRGO/GCE; with a scan rate of 10 mV s–1.
329x140mm (200 x 200 DPI)

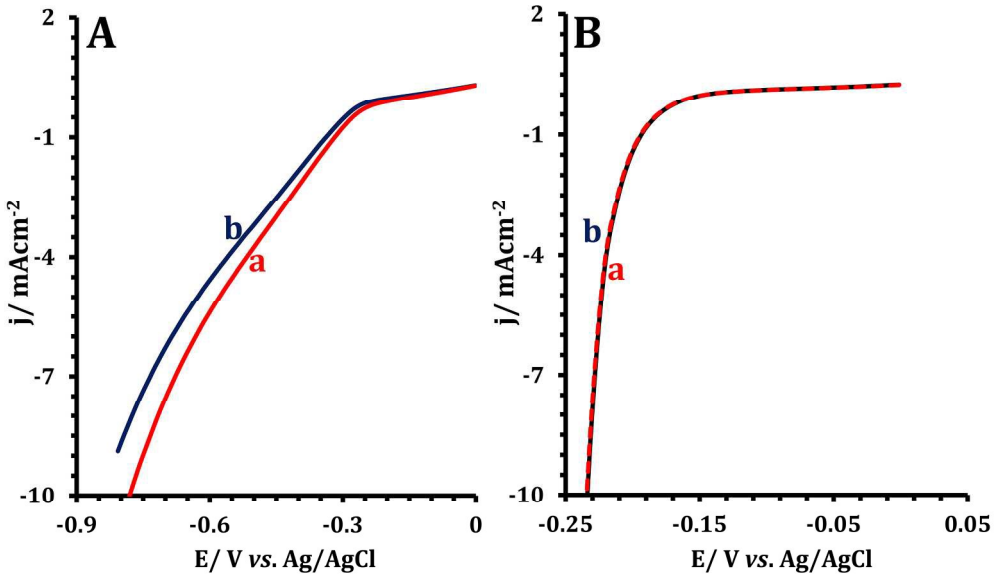

Fig. 8. Long-term electrochemical stability test in 0.5 mol L−1 H2SO4 at A): Nano-PSiF eRGO/GCE, and B): Pt-Pd/PSiF-eRGO/GCE, (a): first cycle, and (b): after 500 cycles; with a scan rate of 10 mV s−1.
307x184mm (200 x 200 DPI)

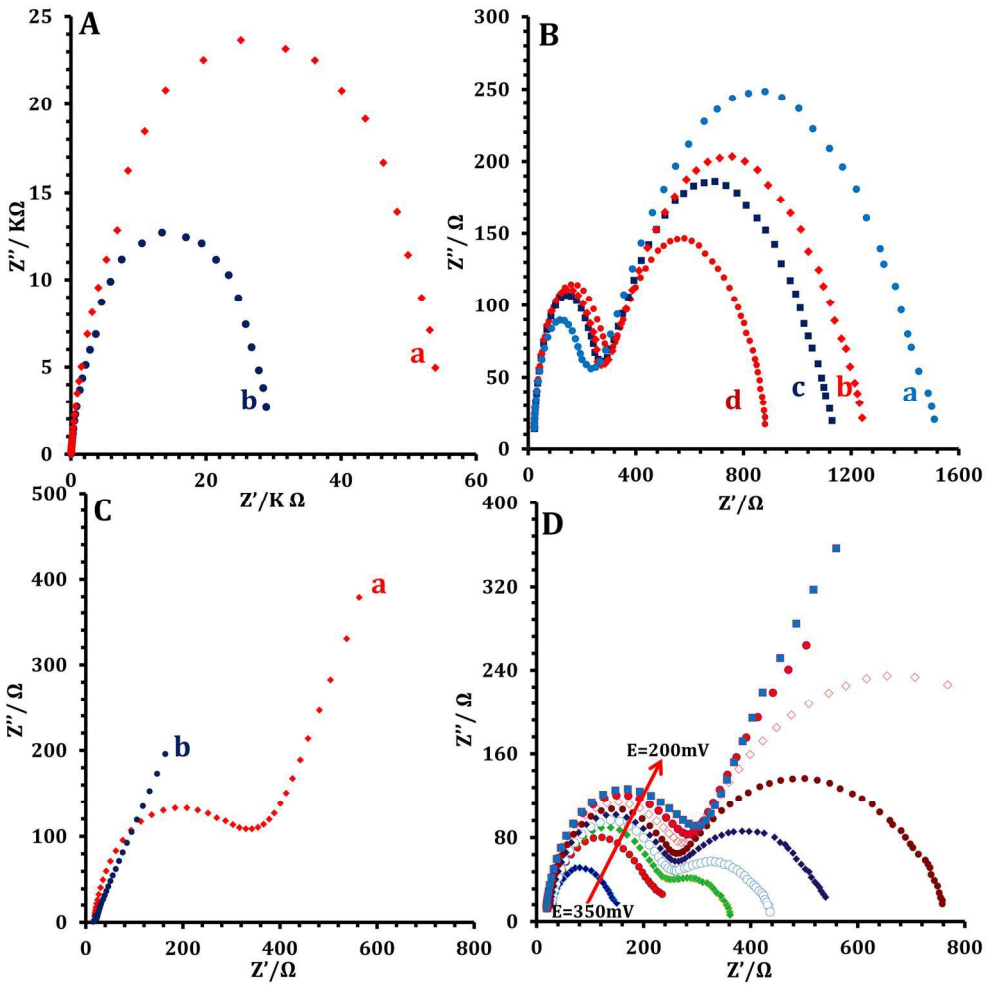

Fig. 9. A): Nyquist plots of a solution containing 0.5 mol L–1 H2SO4 at (a): commercial silicon powder modified GCE; (b): Nano-PSiF modified GCE at potential of 0.40 vs. Ag/AgCl; (B) Nyquist plots of a solution containing 0.5 mol L–1 H2SO4 at (a): Pt/PSiF-GCE; (b): Pt-Ru/PSiF-GCE; (c): Pt-Rh/PSiF-GCE; and (d): Pt-Pd/PSiF-GCE at potential of 0.25 vs. Ag/AgCl; (C) Nyquist plots of a solution containing 0.5 mol L–1 H2SO4 at (a): Pt-Pd/PSiF-GCE; (b): Pt-Pd/PSiF-eRGO/GCE; (D) Nyquist plots of a solution containing 0.5 mol L–1 H2SO4 at Pt-Pd/ PSiF-GCE in different potential of (200, 220, 240, 260, 270, 280, 290, 300, 350 mV) vs. Ag/AgCl in 0.5 mol L–1 H2SO4.
262x262mm (200 x 200 DPI)